Computers in Biology and Medicine 174 (2024) 108401

Contents lists available at ScienceDirect

Computers in Biology and Medicine

journal homepage: www.elsevier.com/locate/compbiomed

Exploring the muscle architecture effect on the mechanical behaviour of mouse rotator cuff muscles

A. Heras-Sádaba [a], A. Pérez-Ruiz [c,d], P. Martins [a], C. Ederra [c,d], C. Ortiz de Solórzano [c,d], G. Abizanda [c,d], J. Pons-Villanueva [c,d,e], B. Calvo [a,b], J. Grasa [a,b,*]

[a] Aragón Institute of Engineering Research (i3A), Universidad de Zaragoza, Spain
[b] Centro de Investigación Biomédica en Red en Bioingeniería, Biomateriales y Nanomedicina (CIBER-BBN), Spain
[c] Technological Innovation Division, Foundation for Applied Medical Research (FIMA), University of Navarra (UNAV), Spain
[d] Instituto de Investigación Sanitaria de Navarra (IdiSNA), Pamplona, Spain
[e] Orthopedic Department, Clínica Universidad de Navarra, Pamplona, Spain

ARTICLE INFO

Keywords:
Mouse rotator cuff
Supraspinatus
Infraspinatus
Muscle architecture
Finite element method

ABSTRACT

Incorporating detailed muscle architecture aspects into computational models can enable researchers to gain deeper insights into the complexity of muscle function, movement, and performance. In this study, we employed histological, multiphoton image processing, and finite element method techniques to characterise the mechanical dependency on the architectural behaviour of supraspinatus and infraspinatus mouse muscles. While mechanical tests revealed a stiffer passive behaviour in the supraspinatus muscle, the collagen content was found to be two times higher in the infraspinatus. This effect was unveiled by analysing the alignment of fibres during muscle stretch with the 3D models and the parameters obtained in the fitting. Therefore, a strong dependence of muscle behaviour, both active and passive, was found on fibre orientation rather than collagen content.

1. Introduction

The musculature of the rotator cuff (RC) plays a crucial role in maintaining the motion and stability of the shoulder joint. It is composed of four muscles, named supraspinatus, infraspinatus, subscapularis and teres minor, which collaborate by ensuring that the humeral head remains securely in the glenoid fossa as they rotate the humeral head in coordination with the periscapular muscles [1,2]. The versatile motion of the shoulder joint regularly subjects the RC to complex and multiaxial loads, meaning that RC is frequently susceptible to injury, resulting in weakness, reduced range of motion, pain and functional limitations. RC degenerative alterations become more prevalent with advancing age, but acute injuries continue to be a concern across all age groups [3,4]. Because of the high frequency of supraspinatus tendon injuries, extensive research has been conducted on supraspinatus muscle anatomy, encompassing aspects such as its musculotendinous structure, imaging characteristics and functional properties. In contrast, there is relatively limited documentation regarding the morphology and function of the infraspinatus muscle in comparison to the supraspinatus, and less attention has been paid to the infraspinatus–supraspinatus relationship [5].

The integrity of RC is intimately linked to its functional behaviour, particularly in terms of muscle force production and movement, which are intricately governed by the muscle's architectural characteristics [6]. Parameters such as fibre bundle length, pennation angle, muscle thickness and cross-sectional area are key factors affecting muscle force properties and function [7–11]. However, decreased flexibility of muscles can determine the success rates of rehabilitation and recovery following RC injury. In this sense, whole muscle stiffness increases when the tendon is torn and as the severity of the tears increases. Despite these observations, it remains a subject of ongoing inquiry whether muscle rigidity primarily arises from fibrotic changes, alterations in the muscle fibres themselves or intricate interactions between collagen content and the disposition of myofibres. Clarifying the precise mechanisms underlying muscle stiffness in RC under physiological condition holds significant implications for understanding RC injuries and improving treatment strategies.

Computational modelling and simulation techniques have become indispensable modern methods for understanding the intricate behaviours and interactions within the musculoskeletal system. These methods offer valuable insights into the functioning, interaction and

* Corresponding author at: Aragón Institute of Engineering Research (i3A), Universidad de Zaragoza, Spain.
E-mail address: jgrasa@unizar.es (J. Grasa).

https://doi.org/10.1016/j.compbiomed.2024.108401
Received 6 December 2023; Received in revised form 15 February 2024; Accepted 1 April 2024
Available online 2 April 2024

contribution of muscles to joint biomechanics and movement generation. However, these models must overcome various challenges to accurately represent the complexity of this system under physiological conditions. To date, only a limited number of computational approaches have integrated multiple muscles into a comprehensive system-level model, and a small subset of simulations has incorporated active 3D models of multiple skeletal muscles [12]. Furthermore, most finite element (FE) models do not consider muscle interactions or detailed anatomical relationships [13]. Basically, they are constrained by the assumption that the muscle-to-muscle contact or the representation of such contact in non-physiological ways [14]. This remains a high computational limitation because architectural variations within muscles hold functional significance [15–17].

In the case of RC muscles, the responses of the infraspinatus and supraspinatus muscles can be influenced by a multitude of factors, including their geometry, locations of origin and insertion, bone and tendon interactions, surrounding structures, boundary and loading conditions, among others. Additionally, numerical modelling applications for RC muscles are severely limited due to the numerous assumptions involved, such as considering a parallel orientation of muscle fibres to the surface. This particular presumption renders the models unsuitable for representing the supraspinatus and infraspinatus muscles, which are pennate muscles. In pennate muscles, fibres run at an angle to the axis of traction which is macroscopically manifested by a single intramuscular tendon, so that the anatomical cross-sectional area does not accurately represent the cross-section perpendicular to all fibres in the muscle. Therefore, it is inadequate to model these muscles using the typical computational musculoskeletal model, which employs the vector component of muscle force exerted along an axis parallel to the length of the tendon [18–21].

The primary objective of this study was to determine the mechanical properties of both the passive and active behaviour of the supraspinatus and infraspinatus mouse muscles, considering their precise architecture. To achieve this goal the study addresses important aspects, including: (i) conducting series of experimental tests to characterise both passive and maximum active isometric force for both muscles; (ii) precise image reconstruction of muscle fibre orientation and external volume; and (iii) employing inverse finite element techniques to find characteristic material parameters for describing the behaviour according to established constitutive models. This will serve as a foundational step in establishing a validated in silico model for diagnosing and performing surgical procedures for shoulder-related dysfunction. It will empower researchers who are evaluating RC tear pathology to investigate functional outcomes and pioneer innovative therapeutic approaches. To present this technique, the paper is structured as follows: the "Materials and Methods" section will provide detailed information regarding tissue processing and characterisation, and evaluation of the mechanical properties of the animal model. Subsequently, the mathematical formulation and the Finite Element program used will be established in the "Computational Model" section. The results will be rigorously analysed in a dedicated "Results" section, followed thorough exploration and interpretation in the "Discussion" section. Finally, the "Conclusions" section will summarise the findings.

2. Materials and methods

2.1. Animal model

Twelve wild-type (WT, C57BL/6J) mice at 12 weeks of age (26.092 ± 0.357 g weight) were purchased from ENVIGO (Ref.: 057; France) and maintained in our Animal housing facilities in compliance with current legislation. After one week, the animals were sacrificed by cervical dislocation to isolate the supraspinatus and infraspinatus muscles for histological ($n = 4$) and mechanical characterisation ($n = 5$) or to obtain the bone–tendon–muscle units from shoulders for further anatomical analyses ($n = 3$).

Sample sizes were determined using the G*Power statistical program, with fixed error ($\alpha = 0.05$) and power ($1 - \beta = 0.9$) parameters, taking into consideration data collected in previous works [22,23].

The study was conducted according to the guidelines of the Declaration of Helsinki, and approved by the Ethics Committee on Experimental Research of the Universidad de Navarra (protocol code 95/19, 11 December 2019). The authors declare no conflict of interest.

2.2. Histological analysis

For histological analyses, the supraspinatus and infraspinatus muscles were fixed in 4% paraformaldehyde (PAF) for 24 h immediately after isolation, washed in PBS and immersed into paraffin. Tissues were serially cut into four longitudinal sections of 4 μm thickness, collected at 400 μm depth intervals throughout the entire muscles.

The tissue sections were washed in PBS, hydrated in grade ethanol and stained with Hematoxylin and Eosin (Merck, Darmstadt, Germany), Masson's Trichromic and Sirius red stainings to reveal the histological structure and the accumulation of collagen.

2.3. Multiphoton analysis

The bone–tendon–muscle units were carefully isolated from mice, fixed in 4% PAF for 48 h and decalcified for 72 h at room temperature (Fig. 1.a). Then, the units were embedded in agarose and longitudinally sectioned in 400-500 μm sections through the entire tissues. A total of 5–6 pieces were collected from each unit (Fig. 1.b-c), maintaining the bone–tendon–muscle connection in any single piece (Fig. 1.d).

Immunostaining of the 400-500 μm bone–tendon–muscle tissue sections for dystrophin (Abcam) was performed after a permeabilisation step with 0.5% Triton X-100/PBS for 24 h at room temperature, followed by several rinses in PBS. Samples were blocked in 10% bovine serum albumine/PBS for 24 h, previous to the addition of primary antibody for another 24 h at room temperature. Dystrophin anti-rabbit antibody was visualised with goat anti-rabbit-488 fluorochrome-conjugated secondary antibody (Molecular Probes). Stained tissue sections were kept in PBS at 4 °C in dark until their use.

After multiphoton microscopy analyses, one of these 400-500 μm pieces was removed from agarose, embedded in paraffin and cut into 4 μm sections at different depth intervals through the whole piece to corroborate tissue architecture of hard and soft tissues within the bone–tendon–muscle units through Hematoxylin and Eosin (Merck, Darmstadt, Germany), Masson's Trichromic and Sirius red stainings.

2.4. Image acquisition

Hematoxylin and Eosin, Masson's Trichromic and Sirius red stained tissue sections were scanned using an automated pathology imaging system.

For multiphoton microscopy image analyses, dystrophin and second harmonic generation (SHG) signals were collected using a Zeiss LSM 880 (Carl Zeiss, Jena, Germany) microscope equipped with a two-photon femtosecond pulsed laser (MaiTai DeepSee, Spectra-Physics, Newport USA), tuned to a central wavelength of 790 nm using a 10×/0.25 objective (LD LCI Plan-Apochromat 10×/0.25, Carl Zeiss, Jena, Germany). Tile and z-stack scans from each 300 μm bone–tendon–muscle sections were acquired at 7.79 μm intervals in non-descanned mode after spectral separation and emission filtering using 380 nm to 430 nm and 465 nm to 515 nm BP filters for SHG and dystrophin signals, respectively. The specific resolution achieved for each image varies, reaching values of up to 20479 × 13311 pixels.

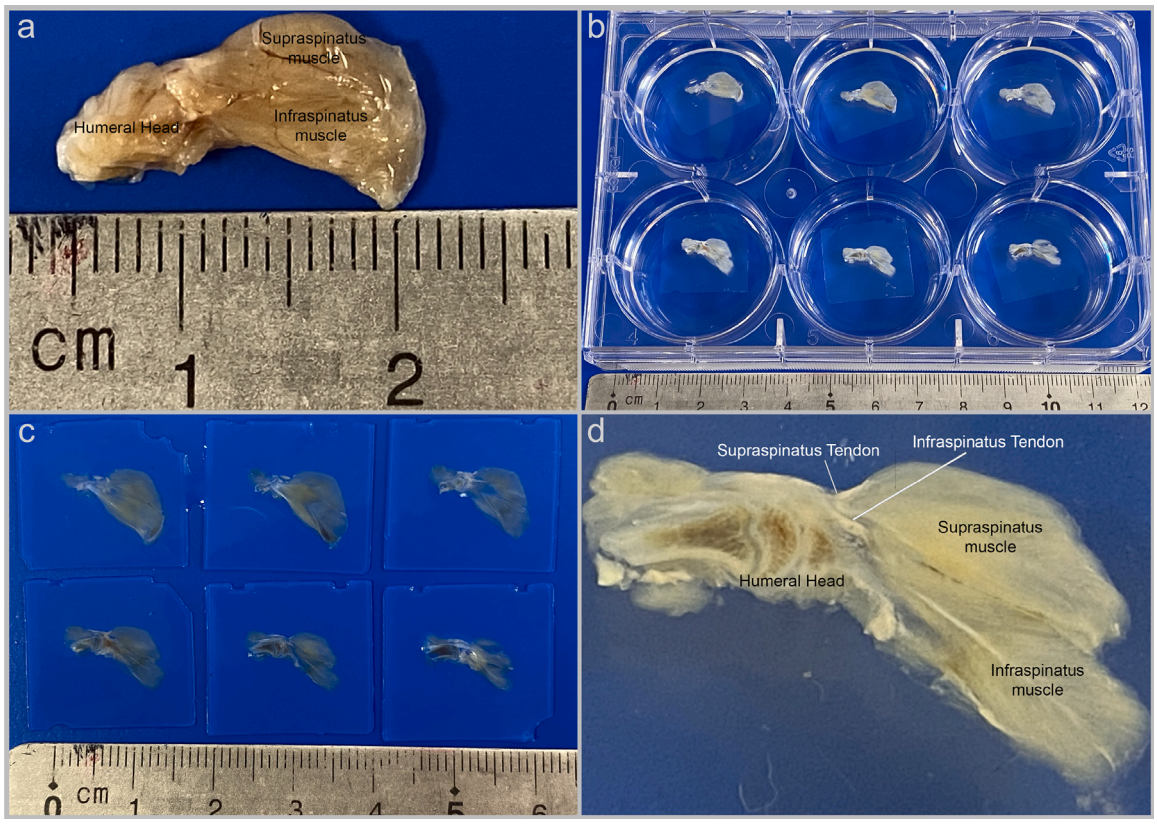

Fig. 1. Details of the sample preparation before observing the tissue sections under the Multiphoton Microscope. (a) Representative image of the fixed bone–tendon–muscle unit after isolation from mice. (b) Collection of the agarose-embedded tissue sections obtained from one mouse. (c) Detail of the agarose-embedded bone–tendon–muscle sections and (d) macroscopic visualisation of the humeral head, supra and infraspinatus tendons and muscles.

2.5. Collagen content analysis

Digital images of Sirius red stainned tissue sections were processed using Fiji software [24] to quantify the collagen content. Positive staining was expressed as the percentage of the stained area divided by the total area of muscle.

2.6. Multiphoton image processing

Using the z-Stack SHG and fluorescent images from multiphoton microscopy, five or six parallel scans were obtained at different depths from each section (Fig. 1.d). This showed the appearance of hard (tendons and bones) and soft (muscles) tissues within the RC. SHG signal channel allowed for detection of the hard tissues, due to their strong SHG responses as consequence of their highly ordered and non-centrosymmetric structures. On the other hand, the green fluorescence channel improved the detection of the weaker SHG signals generated by the muscles, since the sections were immunostained for dystrophin. A different file was saved for each section. Fiji was selected as the image processing tool. In this study, the fluorescent channel to detect soft tissue was selected. As it was commented, the slices of each section revealed the fibre orientations at different depths. All the slices were stacked together to work with only one image that showed the alignment of the muscle fibres for each section. Moreover, the stacked images allowed to reconstruct the whole sample volume, segmenting the contours and fitting a smooth surface to them in SolidWorks.

2.7. Mechanical characterisation

Supraspinatus and infraspinatus muscles from right upper limbs were used to assess passive biomechanical features, while active behaviour of the muscles were analysed in the contralateral limbs.

2.7.1. Passive behaviour

The passive behaviour was studied using an electromechanical Instron Microtester 5248 testing setup (Illinois Tool Works Inc., Glenview, IL, USA), equipped with a 5 N load cell with minimal resolution of 0.001 N. A testing velocity estimated as 0.2 L/100 mm min^{-1}, where L is the initial sample length and 0.2 is the deformation rate, was maintained throughout the test and for all specimens. The whole muscle was tested immediately after sacrificing the animals, either the supraspinatus or the infraspinatus, which were carefully isolated in a retrograde direction, from their tendon insertion into the humeral head to their proximal position in the scapula. For each test, the zero load point was defined after the muscle specimen was clamped at both ends (tendon and scapula). All specimens were subjected to a displacement rate of 3 mm/min until failure. Force and displacement were acquired at 10 Hz and recorded in a data file for further processing.

2.7.2. Active behaviour

The contractile force generation tests used to quantify active behaviour of the muscles were carried out with a 1200 A system (Aurora Scientific Inc. ON, Canada) for in-vitro isolated muscle tests, immediately after sacrificing the animals. Since removing the tissue from the scapula often led to samples unresponsive to the electric field stimulation, a mounting technique that allowed the muscles to remain attached to the scapula (Fig. 2.a) was applied. Both the supraspinatus and infraspinatus tendons were secured using suture (Prolene 6/0, Johnson and Johnson) thread loops and released from their attachment on the humeral head (Fig. 2.b, arrowheads) after removing the acromion and the subscapularis muscle. The dorsal border of the scapula was twice perforated with a needle at the fossa, in the medial borders of the scapula, aligned with the supraspinatus and infraspinatus muscles (Fig. 2.b, arrows) and held with suture thread loops (Fig. 2.c, arrows). Then, the scapula was cut across the spine to isolate the individual

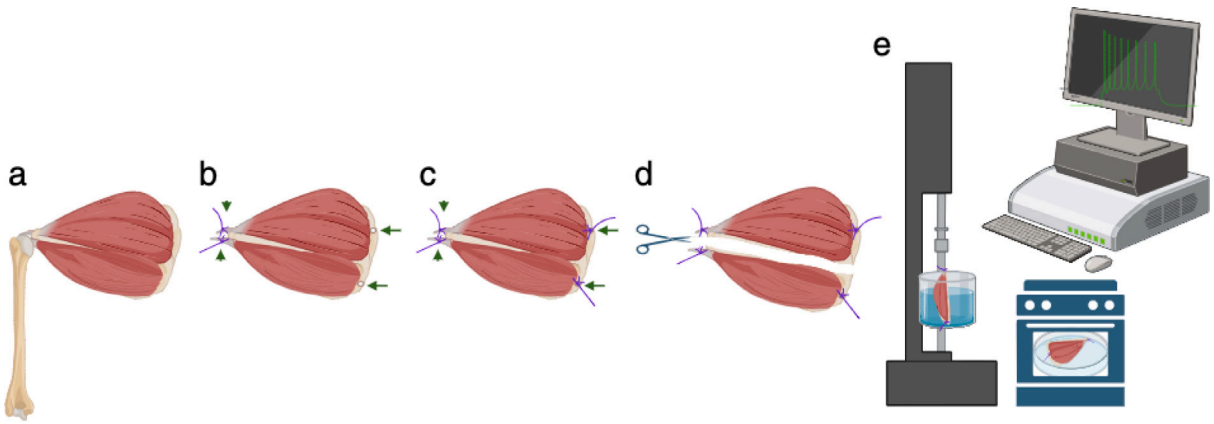

Fig. 2. Scheme of the samples preparation. (a) Supraspinatus and infraspinatus tendons inserted on the humeral head. (b) Free tendons secured with sutures (arrowheads) and holes made on the opposite side of the scapula, in the muscle line of action (arrows), (c) for its next fixation with suture loops (arrows). (d) Then, the scapula was cut across the spine to isolate the individual muscles. (e) Infraspinatus muscles allocated to the contractile device through the sutured ends of the tendon and scapula, keeping the entire structure submerged in a physiological thermal bath. Meanwhile, the supraspinatus muscle was kept in a thermal bath.

muscles (Fig. 2.d) The end of the suture of the infraspinatus tendon was attached to the upper clamp of the device, while the suture end connected to the scapula bone was secured to the lower fixation point (Fig. 2.d), ensuring the proper alignment of the tendon and muscle. The supraspinatus muscle/scapula was kept at 37 °C in Han's balanced medium.

The muscle/scapula sample was maintained on a circulating heated Ringer's solution bath saturated with carbogen gas at 27 °C, using a cylindrical bath chamber (Fig. 2.d). Inside the chamber, the stimulating electrical field required for muscle activation was generated by two electrodes located parallel to the sample. The samples were stimulated by a series of single impulse isometric twitches (1 ms, at 100 V) to determine the optimal length of each sample. To avoid the onset of muscle fatigue, the samples were allowed to rest for 2 min between twitches, with a final resting interval of 5 min. After this process, muscle samples were stimulated with activation frequencies ranging from 10 to 140 Hz (10, 80, 100, 120 and 140 Hz), to induce isometric tetanic contractions. For each frequency, the stimulation was maintained during 0.5 s applying 100 V pulses with 1 ms duration. The samples were rested for 5 min before being stimulated with another frequency. All data from contractile tests (Force (mN), Time (s)) was acquired using a 10 kHz sample frequency.

After testing the infraspinatus muscles, the connections were removed from the device and the suture ends within the supraspinatus tendon and scapula were fixed to the clamps, following the same contractile protocol to analyse the supraspinatus muscle active behaviour.

2.8. Statistical analysis

All statistical analyses were performed using SPSS 15.0 (SPSS Inc.). The Shapiro–Wilk test was used to assess normal distribution. Variables were analysed with the Mann–Whitney U test or Student t tests. All experiments were performed using at least three independent experiments per each condition. Data are expressed as means ± SEM. Values $p < 0.05$ were considered to be statistically significant.

3. Computational model

3.1. Model formulation

The passive and active finite strain response of the muscle was simulated within the framework of continuum mechanics postulating the existence of a strain energy function (SEF) [25]. This function is usually expressed in a decoupled form consisting in a volume-changing and a volume-preserving parts in order to handle the quasi-incompressibility constraint:

$$\Psi = \Psi_{vol} + \bar{\Psi}_p + \bar{\Psi}_a \tag{1}$$

In Eq. (1), $\Psi_{vol} = \frac{\kappa}{2}(J-1)^2$ is the term that accounts for volume-changing deformations with κ the bulk modulus and J being the determinant of the deformation gradient. The SEF, $\bar{\Psi}_p$, used to represent the passive behaviour of the tissue was taken in this work as [26]:

$$\bar{\Psi}_p = c_1\left(\bar{I}_1 - 3\right) + \frac{c_3}{c_4}\left(\exp^{c_4(\bar{I}_4-\bar{I}_{40})} - c_4\left(\bar{I}_4 - \bar{I}_{40}\right) - 1\right) \tag{2}$$

where $\bar{I}_1$ is the first invariant of the symmetric volume-preserve Cauchy–Green tensor, and $\bar{I}_4$ is the pseudo-invariant related to the anisotropy induced by the orientation of the muscle fibres reinforced with collagen tissue. c_1, c_3, c_4 and $\bar{I}_{40}$ are parameters to be determined.

The strain energy $\bar{\Psi}_a$ is associated with the active response and consequently, with the actin–myosin interaction and is expressed as [25]:

$$\bar{\Psi}_a = f_\lambda f_{act}\frac{P_0}{2}(\bar{J}_4 - 1)^2 \tag{3}$$

where P_0 is a proportionality factor related to the maximum active stress due to the muscle contraction. $\bar{J}_4$ is a pseudo-invariant associated to the elastic deformation of the muscle fibres. The functions f_λ and f_{act} are, respectively the influence of filament overlap on the active response of the muscle [27] and the activation function [28].

$$f_\lambda = \exp^{\frac{-(\lambda_a-\lambda_{opt})^2}{2\xi^2}} \qquad f_{act} = \alpha(\tanh\left(A_1(t-t_i)\right))^2(\tanh\left(A_2(t-t_f)\right))^2 \tag{4}$$

λ_a represents the deviatoric part of the muscle fibre stretch. λ_{opt} defines the fibre stretch at which filaments overlap is optimum for force generation and ξ adjusts the horizontal amplitude of the function. $0 \le \alpha \le 1$ is the activation parameter, A_1 and A_2 govern the initial slope starting at $t = t_i$ and the final slope at $t = t_f$ of the activation function.

The formulation of the muscle activation model involves the definition of a contraction or stretch velocity $\dot{\bar{\lambda}}_a$ (see Grasa and Calvo [29] for detailed derivation) which can be obtained as:

$$\dot{\bar{\lambda}}_a = \upsilon_0\left(\frac{\lambda_a - \lambda_{opt}}{2\xi^2}\left(\bar{J}_4 - 1\right)^2 + \frac{2\bar{J}_4\left(\bar{J}_4 - 1\right)}{\lambda_a} - \nu f_{act}\right) \tag{5}$$

where υ_0 is associated with the initial contraction velocity and ν could be interpreted as a friction parameter that takes into account the relative sliding speed between actin and myosin.

In this work, the commercially available finite element software, COMSOL Multiphysics 5.3a, was used to implement the needed equations of the mathematical model. The program uses the classical Galerkin method to obtain an algebraic problem from the set of partial

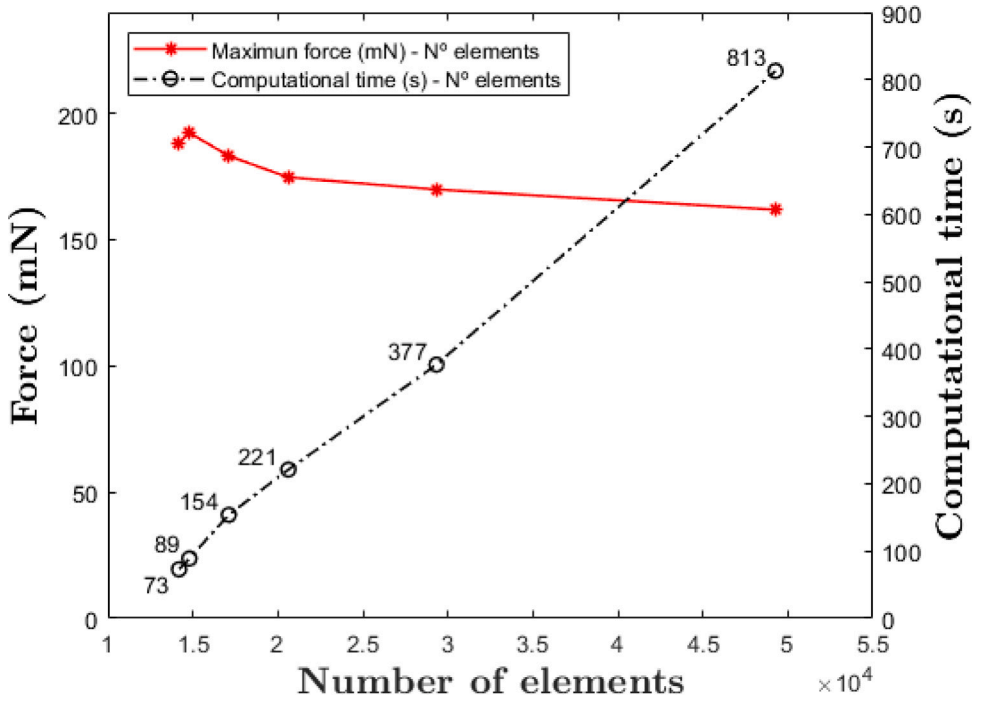

Fig. 3. Relationship between the maximum force developed by the infraspinatus muscle in the model (mN), the number of elements in the mesh, and the computational time (s) required for each simulation.

differential equation system. In each step time increment, the stretch velocity is updated when activation is present ($f_{act} > 0$) and the active fibre stretch computed. Then, the active contribution to the SEF can be obtained updating the elastic deformation of the fibres as $\sqrt{\bar{J}_4} = \lambda\, \lambda_a^{-1}$, with λ the total stretch.

3.2. Finite element model

To find the optimal mesh, a size sensitivity analysis was conducted for both muscle domains. In this analysis, the optimal mesh using the Delaunay-based mesh generator of the program was selected after determining that further refinements did not significantly affect the maximum force developed by the model. The mesh sensitivity analysis is presented in Fig. 3. This figure shows the relationship between the maximum force developed by the infraspinatus muscle in the model, the number of elements in the mesh, and the computational time required for each simulation.

The selected mesh is shown in Fig. 4.a and consists of 5669 nodes and 20616 quadratic serendipity tetrahedral elements. The quality of the mesh was assessed based on the equiangular skew of the elements, and a measure greater than 0.5 was found in all of the mesh elements. No frictional contact was defined between the muscle and bone surfaces, considering the bone domain as a rigid body.

The anisotropy of the tissue was incorporated in the model using the real muscle fibre orientation determined by the image processing as will be shown later. A plain text file, containing the coordinates of the tissue domain together with the components of an orientation vector, was imported into the software. When assembling the matrices to solve the model, the software used this orientation map to interpolate and find the proper fibre direction in every element integration point. In Fig. 4.b these orientations are represented for the infraspinatus muscle. The model incorporated appropriate boundary conditions to simulate the mechanical tests for both muscles, aiming to determine their passive and active behaviour as described previously in the experimental protocols. For the computational simulation of the passive behaviour, one end of the model was attached with a fixed constraint. A displacement of 2 mm was imposed to the opposite end in the loading direction. For the active behaviour both ends were clamped with a fixed constraint, and the isometric contraction was established to recreate the experimental results. This process was performed for both muscles.

4. Results

4.1. Collagen preferably accumulates in the infraspinatus than in supraspinatus muscles of healthy mice

Both the supraspinatus and infraspinatus muscles were isolated from the RC of the mice, longitudinally sectioned, and stained with hematoxylin–eosin (HE), Masson's Trichromic (MT), and Sirius Red (SR) (Fig. 5.a–b). HE staining allowed for the visualisation of the bipennated muscle structure, a feature that became more evident in the MT-stained tissues (Fig. 5.a, c). The latter facilitated the differentiation between tendons and muscles due to the high collagen content in the tendons (Fig. 5.c). This characteristic morphology was further supported by SR staining (Fig. 5.a, c). Furthermore, by using SR staining, we quantified the accumulation of connective tissue in both tissues (Fig. 5.c), and found that the infraspinatus muscles exhibited a significantly higher collagen content compared to the supraspinatus muscles (Fig. 5.d), reflecting a two-fold increase (infra: 4.75 ± 0.71, supra: 2.46 ± 0.32).

4.2. Second harmonic signals accurately compile the RC structure

Multiphoton microscopy images from the bone–tendon–muscle units allowed to visualise the natural position of the glenohumeral joint at the shoulder by the generation of SHG signals. Bone hard tissues, such as humerus and scapula, produced a strong SHG signal (Fig. 6.a) because of their highly ordered and non-centrosymmetric crystalline structure, primarily composed of hydroxyapatite. The supraspinatus tendon, like bones, also produced a strong SHG response and appeared as bright, well-defined structure (Fig. 6.a), due to the densely packed collagen fibres, which have a non-centrosymmetric highly ordered structure. On the other hand, the supraspinatus and infraspinatus soft muscle tissues created weaker but distinct SHG signals (Fig. 6.a), as a

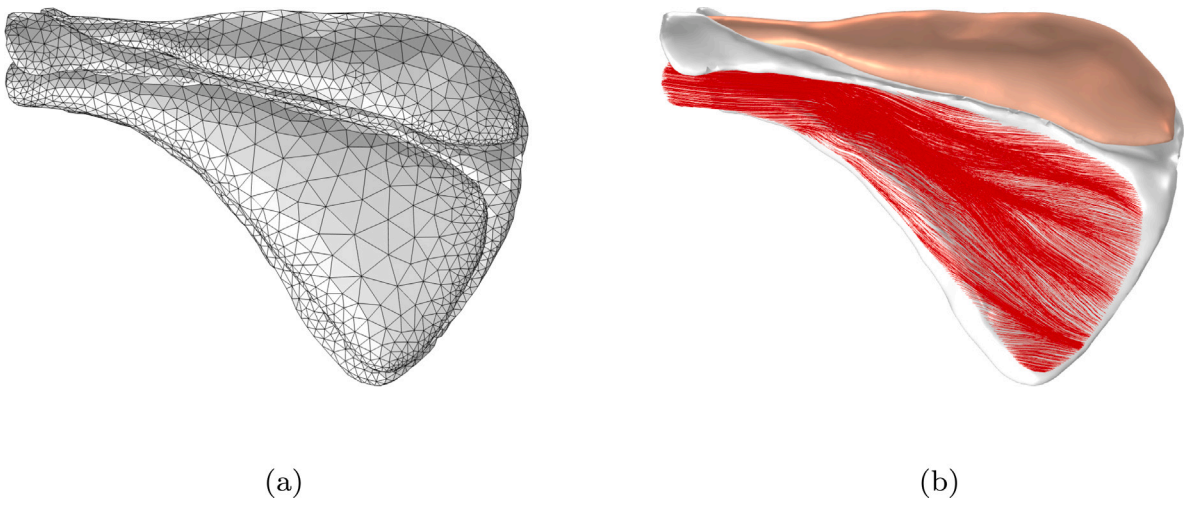

Fig. 4. (a) Finite element mesh used in the model for the scapula and both muscles. (b) Representation of the fibre directions in the infraspinatus muscle.

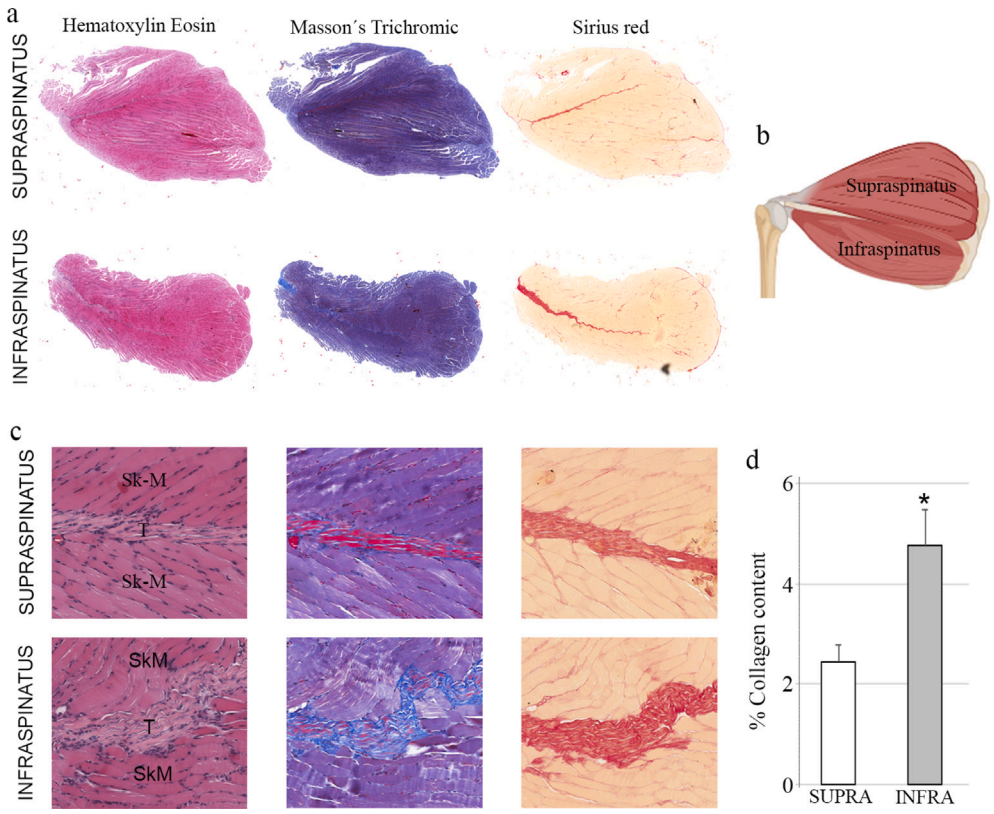

Fig. 5. (a) Representative images of longitudinal supraspinatus and infraspinatus muscle tissue sections stained with hematoxylin-eosin, Masson's trichromic and Sirius red, (b) maintaining their natural position in the RC. (c) High magnification longitudinal images showing the pennated organisation of the muscles and the presence of collagen. (d) Graph shows the accumulation of collagen in the supraspinatus and infraspinatus muscles after staining the tissue sections for Sirius red (mean ± standard deviation of the mean). SK-M, skeletal muscle; T, tendon; SUPRA, supraspinatus muscle; INFRA, infraspinatus muscle.

consequence of their composition of myofibres, which are surrounded and interwoven with collagen fibres, but lack the structural arrangement and organisation found in tendons and bones. Thus, through the analysis of SHG signals, we can visualise the bone–tendon–muscle connections within the RC. Both the supraspinatus and infraspinatus muscles lie on the scapula, separated by its spine, with the supraspinatus tendon running through the supraspinatus muscle before inserting into the top of the humeral head beneath the acromion (Fig. 6a).

HE, MT and SR stainings confirmed the interaction between soft and hard tissues, showing a broad overview of RC microstructure (Fig. 6.b), illustrating the distribution and organisation of collagen and muscle fibres (Fig. 6.c), and providing detailed visualisation of collagen presence (Fig. 6.d), further corroborating the SHG-collagen co-signals. Furthermore, SHG signals acquired at a higher magnification confirmed the pennated characteristic feature of the muscle fibres due to the ordered arrangement of actin and myosin filaments within the myofibres (Fig. 6.e) in both supra and infraspinatus muscles. Meanwhile, dystrophin immunostaining, a specific skeletal muscle marker, helped distinguishing muscle from bone and tendon in images captured at a lower magnification (Fig. 6.f).

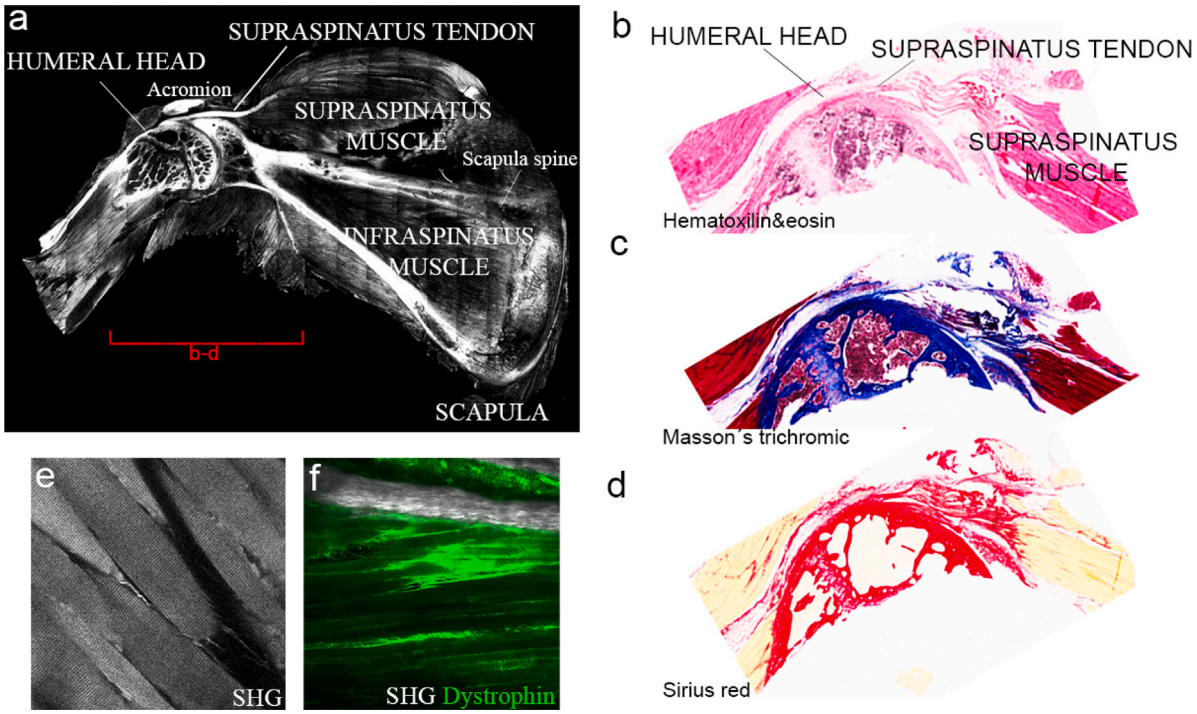

Fig. 6. (a) Representative z-stack projection multiphoton image of agarose-embedded RC bone–tendon–muscle unit from healthy mice, acquired at 10X magnification. (b) Illustrative images of waxed-RC tissue sections stained for hematoxylin–eosin, (c) Masson's trichromic and (d) Sirus red. Images in b-d correspond to the area highlighted in (a). (e) Representative SHG signals from skeletal myofibres acquired at a high magnification (25X). (f) Combination of SHG collagen signals and dystrophin immunostaining acquired at 10X magnification.

4.3. Myofibre pennation angles

The Fiji *Tubeness* plugin [30] was used to process the multiphoton microscopy images (Fig. 7.a). These images were treated as a 3D stack and another set of images were generated where myofibres were transformed to tubular structures. In this plugin, after a few trials, a sigma value of 10 was observed to bring the best results. A comparison between the appearance of the muscle fibres after stacking all the slices (Fig. 7.a) and the appearance of the fibres after applying the *Tubeness* plugin is presented in Fig. 7.b.

Each of the images was imported to Fiji and manipulated separately using the *OrientationJ* plugin and the *Vector Field* method [31]. This plugin examined the images conducting an analysis of the fibre orientations and created a graphic vector field providing a map of coordinates and orientation angles. Fiji *Tubeness* plugin enabled the possibility to obtain the muscle fibre directions. The original data loaded into Fiji showed certain noise and a colour gradient. This prevented *OrientationJ* plugin from properly functioning when applied directly to the stacked slices. An intermediate step was necessary to obtain the muscle fibre directions. This step consisted of applying *Tubeness* plugin. This plugin binarized the previous image and converted the appearance of myofibers into tubular structures, as mentioned before. This enabled the correct application of *Vector Field* option ensuring an accurate interpretation of the binarized image acquiring the fibre orientations. Fig. 7.c shows a detail of the infraspinatus fibre orientations.

After obtaining the vector field of the fibres and their orientation angles, a series of statistical analyses were conducted. First of all, six regions were selected in both muscles as can bee seen in Fig. 8. These regions encompass locations on both sides of the tendon from the proximal to the distal area of the tissues.

Using these regions, the variability of the fibre orientation was assessed for both muscles along the different image sections. This analysis was intended to probe whether or not the directions remained constant in the out of plane direction. One image from the bottom of the stack, one from the middle and another from the top were selected for the three mice samples obtained by the multiphoton microscope. The orientations of the muscle regions were tested initially for normality using the Kolmogórov–Smirnov test, which confirmed the validity of the hypothesis with a p-value greater than 0.05. A one-way ANOVA analysis was performed to determine the similarity of the fibre angles within each region, regardless the section of study. This analysis provided a p-value over 0.01 in all cases proving that the orientation remains constant along the Z-direction for both muscles.

Table 1 shows the mean and standard deviation of the fibre orientations with respect to the central tendon at the different regions.

4.4. Passive behaviour identification

Results for passive experimental tests are shown in Fig. 9.a (mean ± shaded standard deviation). The average evolution of the force registered to conduct an extension of 2 mm in the infraspinatus muscle was of 0.042 ± 0.004 N whereas for the supraspinatus muscle was of 0.075 ± 0.029 N. Infraspinatus muscles weighed 38.4 ± 3 mg in contrast to 42 ± 3 mg of the supraspinatus.

To reproduce the experimental results with the computational model, a prescribed displacement was applied progressively to the tendon end in both muscles until reaching a maximum of 2 mm. With the aim to minimise the difference between the experimental and numerical force–displacement evolution, a series of Monte Carlo simulations were conducted for parameter identification of the SEF associated to the passive behaviour (see Eq. (2)). In these simulations, the parameter range of variation was gradually decreased to reach a coefficient of determination $R^2 > 0.99$. The passive SEF parameters for both muscles are shown in Table 2 and the computational force–displacement evolution curve in Fig. 9.a. The computational time needed for the passive analysis of the infraspinatus was 45 s and for the supraspinatus was 153 s.

4.5. Active behaviour identification

In Fig. 9.b the mean and standard deviation of the experimental active forces obtained for both muscles samples are represented. These

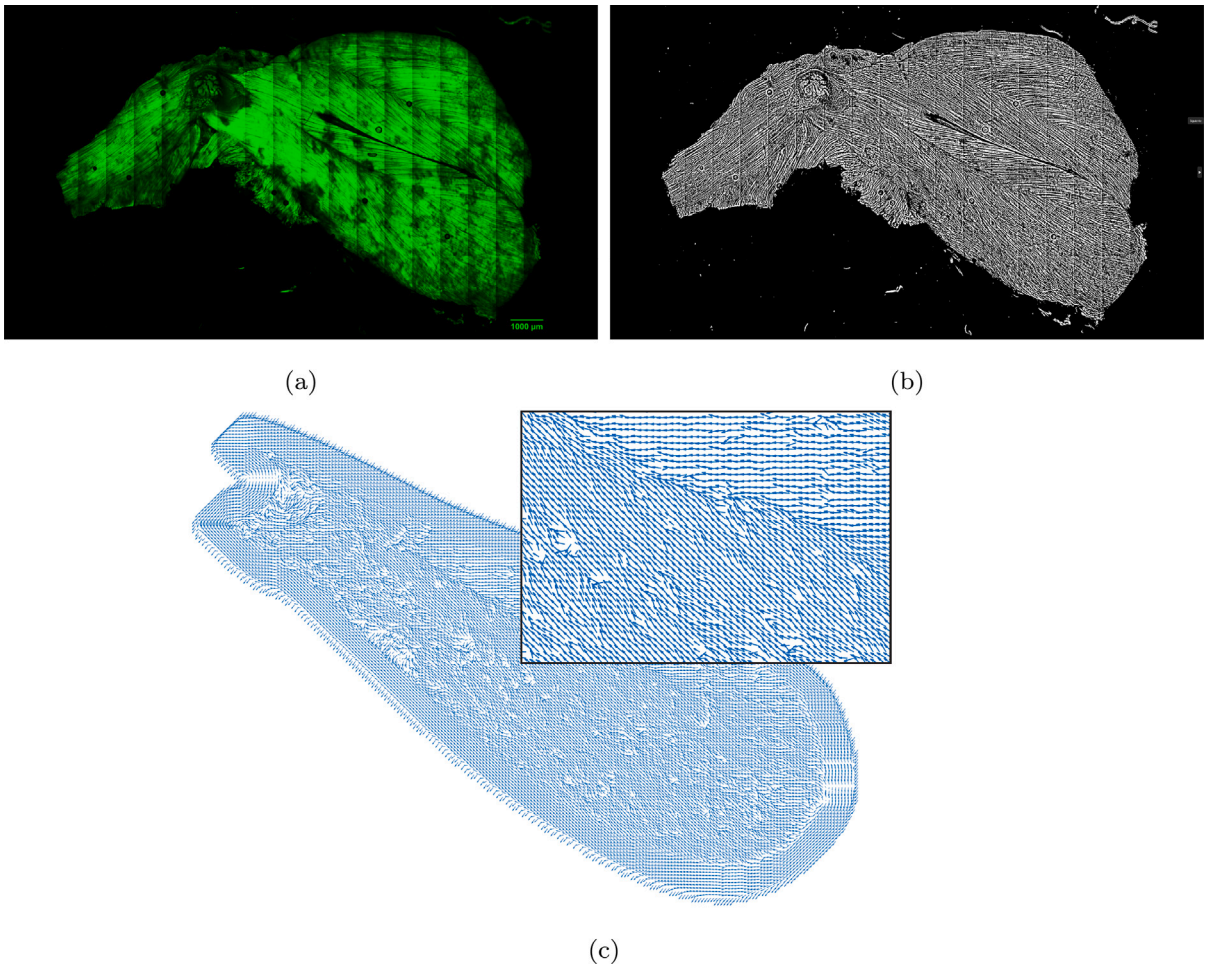

Fig. 7. (a) Appearance of muscle fibres observed under Multiphoton microscope. (b) Threadlike aspect of the muscle fibres after applying *Tubeness* plugin. (c) Representation of infraspinatus fibre orientations after applying *OrientationJ* plugin.

Table 1
Pennation angles (angles of the fibres with respect to central tendon) of the different regions of the infraspinatus and supraspinatus (mean ± standard deviation).

Infraspinatus							Supraspinatus						
	Rg1	Rg2	Rg3	Rg4	Rg5	Rg6		Rg1	Rg2	Rg3	Rg4	Rg5	Rg6
Mean	17.22°	26.60°	5.39°	13.08°	25.46°	17.90°	Mean	7.84°	13.98°	12.03°	14.45°	20.78°	15.84°
Std	±5.36°	±5.63°	±7.43°	±5.70°	±5.26°	±5.92°	Std	±7.20°	±7.47°	±5.64°	±5.76°	±4.83°	±5.92°

Table 2
Parameters for the passive part of the SEF (Eq. (2)).

Infraspinatus				
$\bar{I}_{40}$ [−]	c_1 [MPa]	c_3 [MPa]	c_4 [−]	R^2
1.1	0.0067	0.00022	8.7	0.9992
Supraspinatus				
$\bar{I}_{40}$ [−]	c_1 [MPa]	c_3 [MPa]	c_4 [−]	R^2
1.1	0.0123	0.0012	8.17	0.9989

forces correspond to the maximal isometric tetanic contractions induced by an electrical activation signal of pulses applied at a frequency of 140 Hz. A maximum isometric force of 125.605 ± 47.441 mN at t = 0.2 s was obtained for the supraspinatus muscle whereas for the infraspinatus muscle, a maximum of 176.865 ± 69.501 mN was achieved at t = 0.2 s.

Fixing the tendon end of the computational model, an isometric contraction could be simulated for both muscles. This model allowed to determine the set of parameters associated with the active part of the SEF (Eq. (3)). In a similar way to how it was done in the passive behaviour, a series of simulations, varying those parameters, were conducted to find a coefficient of determination between the experimental and computational curves $R^2 > 0.99$. These parameters are shown in Table 3. The evolution of force over time obtained by the computational model for both muscles is represented in Fig. 9.b. The computational time needed for the active simulations was 221 s for the infraspinatus and 256 s for the supraspinatus.

The developed model could provide useful tools to understand the effect of the muscle architecture in the contraction and force development. Fig. 10.a shows the active stretch λ_a along a representation of muscle fibres when developing the maximum isometric force. In both muscles, at this time point, the more shortened fibres are located at the distal end or tendon region that inserts in the humeral head. The maximum principal stress (Fig. 10.b) is also represented at the same time instant. It can be observed that the maximum principal stresses are located near the insertions whereas in the muscle belly, lower values could be found. In this latter region, during contraction, muscle fibres progressively shorten and rotate decreasing their active stress due to actin and myosin filament overlapping (i.e. force-length relationship).

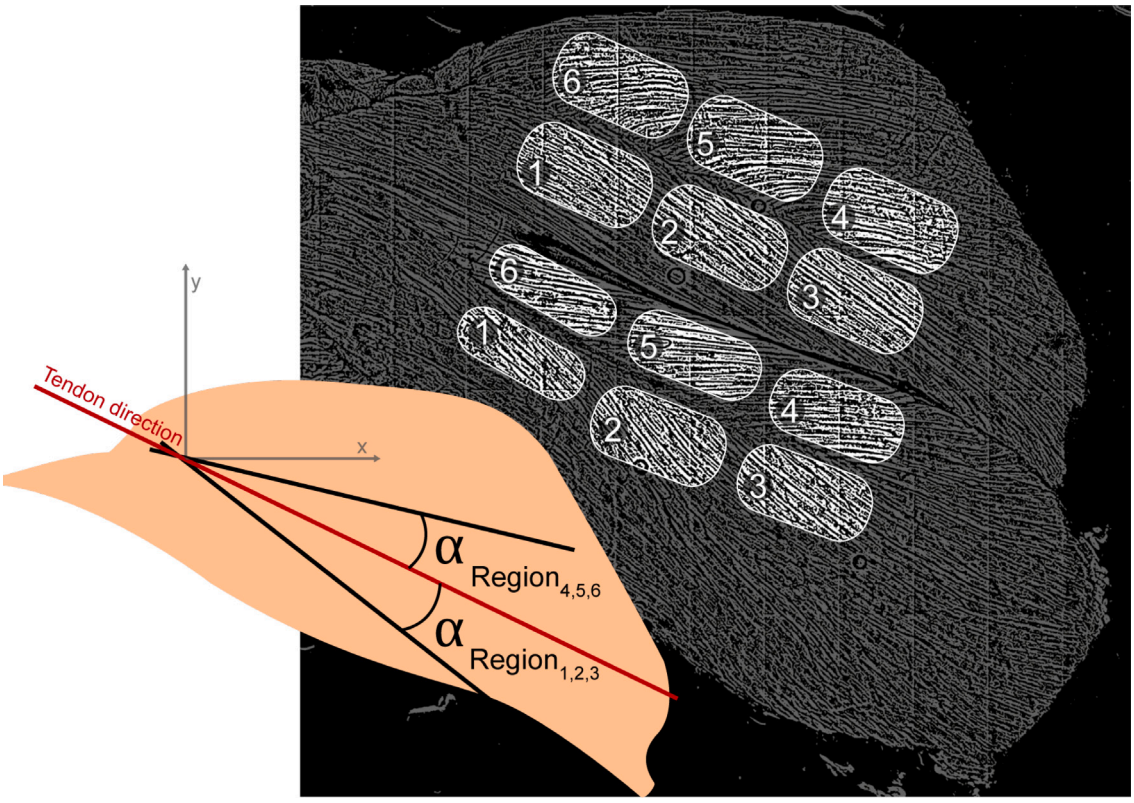

Fig. 8. Regions of the infraspinatus and supraspinatus selected for the statistical analysis and reference system for angle measurements.

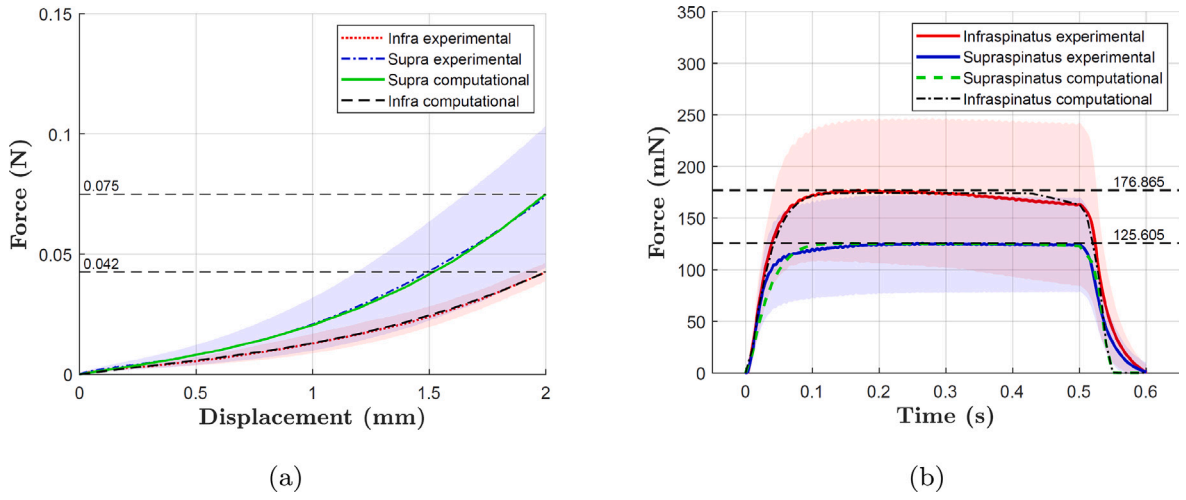

Fig. 9. Curves for experimental and computational results. (a) Force–displacement for the passive response and (b) force-time for the active tetanic isometric contraction.

5. Discussion

Using computational models based on the finite element method to analyse muscle biomechanics, computed tomography (CT) and magnetic resonance imaging (MRI) are common data acquisition techniques used to develop 2D and 3D geometrical models of skeletal muscles [12,27,32–35]. These techniques provide information related to the physiological and anatomical aspects of the entire muscle and its surrounding structures. Consequently, different strategies should be adopted to define the anisotropy of the tissue induced by its architecture such as diffusion tensor-MRI [36]. The Second Harmonic Generation (SHG) imaging technique provides fine-grained, high-resolution images of tissue structures, down to the submicron scale [37]. Thus, it can enhance the visual fidelity and realism of the simulated tissue to generate highly realistic and detailed tissue structures. SHG offers higher spatial resolution than MRI, making it suitable for visualising fine tissue structures and interactions without requiring contrast agents [38]. As found in our study, SHG imaging of mouse RC is highly specific to collagen fibres and other non-centrosymmetric structures, enabling targeted visualisation of collagen-related structures, such as tendons and bones [39]. Since collagen is present in the endomysium and perimysium connective tissue of muscle, our imaging of collagen fibres indirectly revealed the orientation of muscle myofibres, as they align with the collagen structures. This advantage allowed us to discern between the supraspinatus and infraspinatus muscles, which are adjacent to the scapula and separated by the scapular spine. It provided a fine microscale imaging of muscle connections through the supraspinatus tendon and the humeral head. Furthermore, this level of detail was

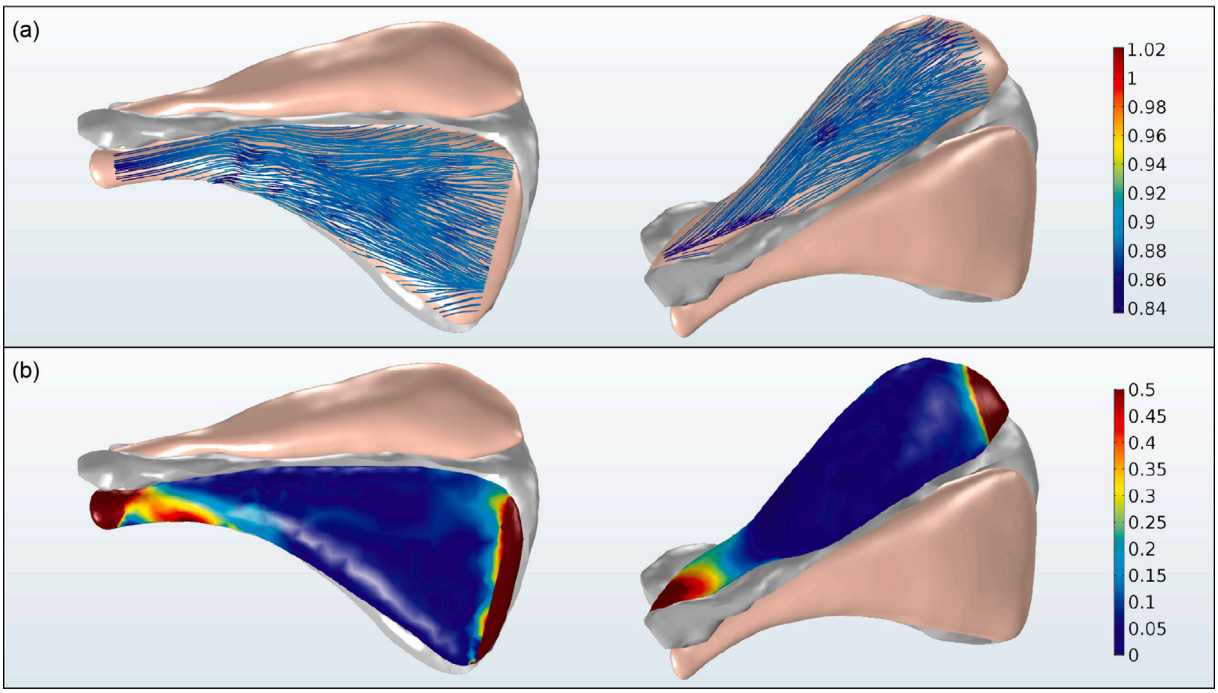

Fig. 10. (a) Active stretch λ_a represented along the fibre orientations at $t = 0.2$ s for infraspinatus (left) and supraspinatus (right). (b) Contour plot of the first principal stress (MPa) at $t = 0.2$ s for infraspinatus (left) and supraspinatus (right).

Table 3
Parameters determined from the fitting of the 3D models to the mean of the experimental tetanic contraction under isometric conditions.

	Infraspinatus	Supraspinatus
Force–stretch relationship		
λ_{opt} [–]	1	1
ξ	0.16384	0.16384
Force Time relationship		
A_1 [–]	180	200
A_2 [–]	53	61
Active SEF		
P_0 (MPa)	0.42	0.363
v_0 (s^{-1})	6	6
ν [–]	0.59	0.59
Goodness of fit		
R^2	0.9762	0.9745

crucial for accurately visualising the orientation and arrangement of muscle fibres, enabling the quantification of individual myofibres and their pennation angles.

The use of SHG imaging has allowed not only to determine supraspinatus and infraspinatus architecture, but also their whole geometry with high accuracy. Although sections of 500 μm were obtained for each muscle, the microscope captured images every 7.79 μm which, after segmentation, provided the external contour delimiting the tissues. This process for generating the 3D muscle domains has a limitation regarding the upper part not in contact with the bone where segmentation turned to be quite difficult. In this region, the fitting surface was chosen smooth enough to close the muscle volume with no visual discrepancy to the real tissue. As described previously, when characterising their passive mechanical behaviour, the muscles were tested entirely. This procedure was adopted due to the impossibility of extracting regular shaped samples of the tissue to guarantee uni-axial loading. Therefore, a technique based on finite element simulations [40] allowed to find an anisotropic hyperelastic constitutive law and to determine their characteristic parameters. To the best of authors' knowledge, no previous research results on the passive behaviour of supraspinatus and infraspinatus muscles could be found in the literature. In the work of Smith and Barton [41], muscles from the lower limb (Extensor digitorum longus and soleus muscle) were tested passively in the physiological range of deformation. They reported higher collagen content for the mouse control group and a global stiffness value representing the passive behaviour. Although these results cannot be compared, they are in the same order of magnitude as parameter c_1 in our proposed SEF which represents the stiffness at a lower strain range. Studies where constitutive laws are formulated for computational simulation purposes, i.e. finite element models, are only reported for other species and muscle tissues [26,27,42]. The proposed technique to determine SEF parameters is not exempt from limitations since the models are developed with a geometry that is not the one used in the real experiment. This limitation may not be critical since the average behaviour is analysed and animals were carefully selected regarding age and weight and consequently tissue dimensions.

In the work of Valencia et al. [43], contractility of the supraspinatus muscle was analysed in mice of the same age and weight. They reported values of 260 ± 30 mN for tetanic contractions that are larger than the results in our study (125.6 ± 47 mN). Differences could be found in the experimental protocol, since Valencia et al. [43] used an in-vivo setup while in our work in-vitro tests were conducted. The dissection and manipulation time of muscles may influence cellular processes within the muscle tissue, potentially resulting in an underestimation of the maximum tetanic force of the supraspinatus. This is particularly noteworthy in our study when analysing the supraspinatus subsequent to the infraspinatus and despite resting times between stimulus, fatigue may appear. On the other hand, no maximum tetanic force has been reported in the literature for mouse infraspinatus muscles. Based on the muscle weight measurements, the infraspinatus exhibits a weight approximately 9% lighter than the supraspinatus. Despite that, the infraspinatus muscle developed a greater maximum tetanic force compared to the supraspinatus. As observed, pennation angles in the infraspinatus muscle are larger than those for the supraspinatus. It is well known that the force produced by pennate muscles is greater than the force produced by parallel muscles [44]. Therefore, as demonstrated in the analysis of the two muscles, the higher the pennation

angles, the greater the force, despite having less mass. This effect is also contemplated and predicted by the computational modelling. The parameters obtained for both muscles differs basically in those related to the force time relationship. The initial and final slopes for the infraspinatus muscle are lower, indicating a longer time to reach the maximum isometric force and to relax, respectively. It is noteworthy to mention that the model does not contemplate the metabolic behaviour of muscle fibres and only predicts an average behaviour. Moreover, slight differences are noted in the results of the model at the end of the contraction phase in both muscles, as evidenced by the goodness of fit.

While the computational model may be properly calibrated with suitable parameters for isometric contractions, it retains the ability to simulate additional physiological scenarios. However, it is important to note that these additional scenarios, such as concentric and eccentric contractions, have not been explicitly tested. However, to faithfully replicate concentric and eccentric contractions, it becomes imperative to integrate additional relationships into the strain–energy function such as the dependence with the velocity of contraction. Furthermore, further experimental tests are necessary to validate the model in these scenarios.

Our study showed that the infraspinatus muscles exhibit a higher collagen content than their supraspinatus counterparts, yet the former is less stiff. Regarding collagen content this result is in agreement with that observed in humans where the insertion area of the infraspinatus is clearly larger than that of the supraspinatus [45]. Likewise, it is known that for the development of mechanical dysfunction in cuff rupture, there must be involvement of the infraspinatus; isolated rupture of the supraspinatus is not sufficient [46]. Also clinical experience has allowed to observe the importance of the pennation angle in the prognosis of RC injuries [11]. As it has been demonstrated, the finite element model accounting for the real fibre orientations allowed to understand how in both passive and active simulations, pennation angle reduces progressively orientating the fibres in the loading direction. Taking into account the inherent differences between species that may limit direct extrapolation to humans, after geometry and model parameters, the methodology presented could provide future insights into the prognosis of injuries once the angle of pennation is known. In cases in which it is not possible to repair the infraspinatus, the palliative option with latissimus dorsi or lower trapezius transfer is considered. Beyond the vectorial possibilities of each transfer, it would be necessary to compare which would be more convenient in this aspect [47].

6. Conclusions

The study of the architecture of the mouse RC muscles supraspinatus and infraspinatus has unveiled the important effect of the pennation angle on their mechanical behaviour. The information provided by the multiphoton microscopy has contributed to elaborate an accurate muscle fibre mapping to develop suitable computational models. The parameters obtained from fitting these 3D models, along with their proven robustness, can be used for further analysis of shoulder biomechanics.

CRediT authorship contribution statement

A. Heras-Sádaba: Writing – original draft, Software, Investigation. **A. Pérez-Ruiz:** Writing – review & editing, Writing – original draft, Supervision, Project administration, Methodology, Investigation, Funding acquisition, Data curation, Conceptualization. **P. Martins:** Writing – review & editing, Investigation, Data curation, Conceptualization. **C. Ederra:** Investigation, Data curation. **C. Ortiz de Solórzano:** Writing – review & editing, Investigation, Data curation. **G. Abizanda:** Writing – review & editing, Supervision, Methodology, Investigation, Conceptualization. **J. Pons-Villanueva:** Writing – review & editing, Supervision, Methodology, Investigation, Conceptualization. **B. Calvo:** Writing – review & editing, Writing – original draft, Supervision, Methodology, Investigation, Conceptualization. **J. Grasa:** Writing – review & editing, Writing – original draft, Validation, Supervision, Software, Project administration, Methodology, Investigation, Data curation, Conceptualization.

Declaration of competing interest

The authors declare the following financial interests/personal relationships which may be considered as potential competing interests: Jorge Grasa reports financial support was provided by University of Zaragoza. Jorge Grasa reports a relationship with Spain Ministry of Science and Innovation that includes: funding grants. Ana Perez-Ruiz reports a relationship with Spain Ministry of Science and Innovation that includes: funding grants. If there are other authors, they declare that they have no known competing financial interests or personal relationships that could have appeared to influence the work reported in this paper.

Acknowledgements

Research support was provided by the Spanish Ministerio de Ciencia, Innovación *y* Universidades (Grant PID2020-113822RB-C21 and PID2020-113822RB-C22) and the Department of Industry and Innovation (Government of Aragon) through the research group Grant T24-20R (cofinanced by Feder). Part of the work was performed by the ICTS "NANBIOSIS" specifically by the Tissue and Scaffold Characterization Unit (U13) of the CIBER in Bioengineering, Biomaterials & Nanomedicine (CIBER-BBN at the University of Zaragoza). CIBER actions are financed by the Instituto de Salud Carlos III, Spain with assistance from the European Regional Development Fund. We also thank to Leire Extramiana, Ainhoa Urbiales, Carolina Gorrin and Purificación Ripalda Cemborain for their technical support during tissue processing and image acquisition.

References

[1] E. Itoi, H.C. Hsu, K.N. An, Biomechanical investigation of the glenohumeral joint, J. Shoulder Elb. Surg. 5 (1996) 407–424, http://dx.doi.org/10.1016/S1058-2746(96)80074-7.
[2] J. Hurov, Anatomy and mechanics of the shoulder: review of current concepts, J. Hand. Ther. 22 (2009) 328–342, http://dx.doi.org/10.1016/j.jht.2009.05.002.
[3] A. Yamamoto, K. Takagishi, T. Osawa, T. Yanagawa, D. Nakajima, H. Shitara, T. Kobayashi, Prevalence and risk factors of a rotator cuff tear in the general population, J. Shoulder Elb. Surg. 19 (2010) 116–120, http://dx.doi.org/10.1016/j.jse.2009.04.006.
[4] R.Z. Tashjian, Epidemiology, natural history, and indications for treatment of rotator cuff tears, Clin. Sports Med. 31 (2012) 589–604, http://dx.doi.org/10.1016/j.csm.2012.07.001.
[5] A. Kato, A. Nimura, K. Yamaguchi, T. Mochizuki, H. Sugaya, K. Akita, An anatomical study of the transverse part of the infraspinatus muscle that is closely related with the supraspinatus muscle, Surg. Radiol. Anat. 34 (2012) 257–265, http://dx.doi.org/10.1007/s00276-011-0872-0.
[6] R.L. Lieber, J. Fridén, Clinical significance of skeletal muscle architecture, Clin. Orthop. Relat. Res. 14 (2001) 0–151, http://dx.doi.org/10.1097/00003086-200102000-00016.
[7] S.H. Scott, D.A. Winter, A comparison of three muscle pennation assumptions and their effect on isometric and isotonic force, J. Biomech. 24 (1991) 163–167, http://dx.doi.org/10.1016/0021-9290(91)90361-P.
[8] M. Narici, Human skeletal muscle architecture studied in vivo by non-invasive imaging techniques: functional significance and applications, J. Electromyography Kinesiology 9 (1999) 97–103, http://dx.doi.org/10.1016/S1050-6411(98)00041-8.
[9] T.D. Boehm, S. Kirschner, T. Mueller, U. Sauer, F.E. Gohlke, Dynamic ultrasonography of rotator cuff muscles, J. Clin. Ultrasound 33 (2005) 207–213, http://dx.doi.org/10.1002/jcu.20124.
[10] S. Kim, R. Bleakney, E. Boynton, K. Ravichandiran, T. Rindlisbacher, N. McKee, A. Agur, Investigation of the static and dynamic musculotendinous architecture of supraspinatus, Clin. Anat. 23 (2010) 48–55, http://dx.doi.org/10.1002/ca.20896.
[11] I. Hayashi, M. Enokida, K. Nagira, T. Yamasita, Y. Tsukutani, T. Murakami, H. Nagashima, Change in the pennation angle of the supraspinatus muscle after rotator cuff tear repair, J. Shoulder Elb. Surg. 28 (2019) 888–892, http://dx.doi.org/10.1016/j.jse.2018.10.021.

[12] T.T. Dao, M.C.H.B. Tho, A systematic review of continuum modeling of skeletal muscles: Current trends, limitations, and recommendations, Appl. Bionics Biomech. 2018 (2018) 1–17, http://dx.doi.org/10.1155/2018/7631818.
[13] L.A. Spyrou, N. Aravas, Muscle-driven finite element simulation of human foot movements, Comput. Methods Biomech. Biomed. Eng. 15 (2012) 925–934, http://dx.doi.org/10.1080/10255842.2011.566564.
[14] J.W. Fernandez, P.J. Hunter, An anatomically based patient-specific finite element model of patella articulation: towards a diagnostic tool, Biomech. Model Mechanobiol. 4 (2005) 20–38, http://dx.doi.org/10.1007/s10237-005-0072-0.
[15] H.H. Savelberg, H.C. Schamhardt, The influence of inhomogeneity in architecture on the modelled force-length relationship of muscles, J. Biomech. 28 (1995) 187–197, http://dx.doi.org/10.1016/0021-9290(94)00050-e.
[16] A.M. Agur, V. Ng-Thow-Hing, K.A. Ball, E. Fiume, N.H. McKee, Documentation and three-dimensional modelling of human soleus muscle architecture, Clin. Anat. 16 (2003) 285–293, http://dx.doi.org/10.1002/ca.10112.
[17] B. Bolsterlee, T. Finni, A. D'Souza, J. Eguchi, E.C. Clarke, R.D. Herbert, Three-Dimensional Architecture of the Whole Human Soleus Muscle in Vivo, vol. 6, PeerJ, 2018, p. e4610, http://dx.doi.org/10.7717/peerj.4610.
[18] J.H. Challis, D.G. Kerwin, Determining individual muscle forces during maximal activity: Model development, parameter determination, and validation, Hum. Mov. Sci. 13 (1994) 29–61, http://dx.doi.org/10.1016/0167-9457(94)90028-0.
[19] S.L. Winter, J.H. Challis, The expression of the skeletal muscle force-length relationship in vivo: A simulation study, J. Theoret. Biol. 262 (2010) 634–643, http://dx.doi.org/10.1016/j.jtbi.2009.10.028.
[20] S.L. Winter, J.H. Challis, The force-length curves of the human rectus femoris and gastrocnemius muscles in vivo, J. Appl. Biomech. 26 (2010) 45–51, http://dx.doi.org/10.1123/jab.26.1.45.
[21] E.M. Arnold, S.R. Hamner, A. Seth, M. Millard, S.L. Delp, How muscle fiber lengths and velocities affect muscle force generation as humans walk and run at different speeds, J. Exp. Biol. 216 (2013) 2150–2160, http://dx.doi.org/10.1242/jeb.075697.
[22] J. Grasa, A. Pérez-Ruíz, M. Muñoz, F. Soteras, M. Bobadilla Muñoz, A.Baraibar. Churio, F. Prósper, B. Calvo, A quantitative method for the detection of muscle functional active and passive behavior recovery in models of damage-regeneration, Proc. Inst. Mech. Eng. L 233 (2019) 1594–1603, http://dx.doi.org/10.1177/1464420718765312.
[23] L. Gil-Melgosa, J. Grasa, A. Urbiola, R. Llombart, M.S. Ruiz, V. Montiel, C. Ederra, B. Calvo, M. Ariz, P. Ripalda-Cemborain, F. Prosper, C.O. de Solórzano, J. Pons-Villanueva, A.P. Ruiz, Muscular and tendon degeneration after achilles rupture: New insights into future repair strategies, Biomedicines 10 (19) (2021) http://dx.doi.org/10.3390/biomedicines10010019.
[24] J. Schindelin, I. Arganda-Carreras, E. Frise, V. Kaynig, M. Longair, T. Pietzsch, S. Preibisch, C. Rueden, S. Saalfeld, B. Schmid, J.Y. Tinevez, D.J. White, V. Hartenstein, K. Eliceiri, P. Tomancak, A. Cardona, Fiji: An open-source platform for biological-image analysis, Nature Methods 9 (2012) 676–682, http://dx.doi.org/10.1038/nmeth.2019.
[25] B. Hernández-Gascón, J. Grasa, B. Calvo, J. Rodríguez, A 3d electro-mechanical continuum model for simulating skeletal muscle contraction, J. Theoret. Biol. 335 (2013) 108–118, http://dx.doi.org/10.1016/j.jtbi.2013.06.029.
[26] J. Grasa, M. Sierra, N. Lauzeral, M. Muñoz, F. Miana-Mena, B. Calvo, Active behavior of abdominal wall muscles: Experimental results and numerical model formulation, J. Mech. Behav. Biomed. Mater. 61 (2016) 444–454, http://dx.doi.org/10.1016/j.jmbbm.2016.04.013.
[27] J. Grasa, A. Ramírez, R. Osta, M.J. Muñoz, F. Soteras, B. Calvo, A 3D active-passive numerical skeletal muscle model incorporating initial tissue strains. validation with experimental results on rat tibialis anterior muscle, Biomech. Model. Mechanobiol. 10 (2011) 779–787, http://dx.doi.org/10.1007/s10237-010-0273-z.
[28] I. Cabeza-Gil, J. Grasa, B. Calvo, A validated finite element model to reproduce helmholtz's theory of accommodation: a powerful tool to investigate presbyopia, Ophthalmic Physiol. Opt. 41 (2021) 1241–1253, http://dx.doi.org/10.1111/opo.12876.
[29] J. Grasa, B. Calvo, Simulating extraocular muscle dynamics. a comparison between dynamic implicit and explicit finite element methods, Mathematics 9 (2021) http://dx.doi.org/10.3390/math9091024, URL https://www.mdpi.com/2227-7390/9/9/1024.
[30] M. Longair, S. Preibisch, J. Schindelin, Tubeness plugin for ImageJ, 2023, https://www.longair.net/edinburgh/imagej/tubeness/. (Accessed 4 November 2023).
[31] R. Rezakhaniha, A. Agianniotis, J.T. Schrauwen, A. Griffa, D. Sage, C.V. Bouten, F.N.V.D. Vosse, M. Unser, N. Stergiopulos, Experimental investigation of collagen waviness and orientation in the arterial adventitia using confocal laser scanning microscopy, Biomech. Model Mechanobiol. 11 (2012) 461–473, http://dx.doi.org/10.1007/s10237-011-0325-z.
[32] J. Grasa, M. Sierra, M.J. Muñoz, F. Soteras, R. Osta, B. Calvo, F.J. Miana-Mena, On simulating sustained isometric muscle fatigue: a phenomenological model considering different fiber metabolisms, Biomech. Model Mechanobiol. 13 (2014) 1373–1385, http://dx.doi.org/10.1007/s10237-014-0579-3.
[33] B. Hernández-Gascón, E. Peña, J. Grasa, G. Pascual, J.M. Bellón, B. Calvo, Mechanical response of the herniated human abdomen to the placement of different prostheses, J. Biomech. Eng. 135 (51004) (2013) http://dx.doi.org/10.1115/1.4023703.
[34] B. Babaei, D. Fovargue, R.A. Lloyd, R. Miller, L. Jugé, M. Kaplan, R. Sinkus, D.A. Nordsletten, L.E. Bilston, Magnetic resonance elastography reconstruction for anisotropic tissues, Med. Image Anal. 74 (2021) 102212, http://dx.doi.org/10.1016/j.media.2021.102212.
[35] M. Karami, H. Zohoor, B. Calvo, J. Grasa, A 3d multi-scale skeletal muscle model to predict active and passive responses. application to intra-abdominal pressure prediction, Comput. Methods Appl. Mech. Engrg. 415 (2023) 116222, http://dx.doi.org/10.1016/j.cma.2023.116222.
[36] J. Varvik, T.F. Besier, G.G. Handsfield, Computational fluid dynamics simulations for 3d muscle fiber architecture in finite element analysis: Comparisons between computational fluid dynamics and diffusion tensor imaging, Int. J. Numer. Method Biomed. Eng. 37 (2021) e3521, http://dx.doi.org/10.1002/cnm.3521.
[37] C.P. Pfeffer, B.R. Olsen, F. Ganikhanov, F. Légaré, Imaging skeletal muscle using second harmonic generation and coherent anti-stokes raman scattering microscopy, Biomed. Opt. Express 2 (2011) 1366–1376, http://dx.doi.org/10.1364/BOE.2.001366.
[38] N. Hennessy, C. Simms, Skeletal muscle extracellular matrix structure under applied deformation observed using second harmonic generation microscopy, Acta Biomater. (2023) http://dx.doi.org/10.1016/j.actbio.2023.09.047.
[39] E. Hase, K. Sato, D. Yonekura, T. Minamikawa, M. Takahashi, T. Yasui, Evaluation of the histological and mechanical features of tendon healing in a rabbit model with the use of second-harmonic-generation imaging and tensile testing, Bone Jt. Res. 5 (2016) 577–585, http://dx.doi.org/10.1302/2046-3758.511.BJR-2016-0162.R1.
[40] M. Sierra, F.J. Miana-Mena, B. Calvo, J.F. Muñoz, J. Grasa, On using model populations to determine mechanical properties of skeletal muscle. application to concentric contraction simulation, Ann. Biomed. Eng. 43 (2015) 2444–2455, http://dx.doi.org/10.1007/s10439-015-1279-6.
[41] L.R. Smith, E.R. Barton, Collagen content does not alter the passive mechanical properties of fibrotic skeletal muscle in mdx mice, Am. J. Physiol. Cell Physiol. 306 (2014) C889–98, http://dx.doi.org/10.1152/ajpcell.00383.2013.
[42] B. Calvo, A. Ramírez, A. Alonso, J. Grasa, F. Soteras, R. Osta, M. Muñoz, Passive nonlinear elastic behaviour of skeletal muscle: Experimental results and model formulation, J. Biomech. 43 (2010) 318–325, http://dx.doi.org/10.1016/j.jbiomech.2009.08.032.
[43] A.P. Valencia, S.R. Iyer, S.J.P. Pratt, M.N. Gilotra, R.M. Lovering, A method to test contractility of the supraspinatus muscle in mouse, rat, and rabbit, J. Appl. Physiol. 120 (2016) 310–317, http://dx.doi.org/10.1152/japplphysiol.00788.2015.
[44] B. MacIntosh, P. Gardiner, A. McComas, Skeletal muscle: Form and function, 2006, Human Kinetics.
[45] T. Mochizuki, H. Sugaya, M. Uomizu, K. Maeda, K. Matsuki, I. Sekiya, T. Muneta, K. Akita, Humeral insertion of the supraspinatus and infraspinatus. new anatomical findings regarding the footprint of the rotator cuff, J. Bone Joint Surg. Am. 90 (2008) 962–969, http://dx.doi.org/10.2106/JBJS.G.00427.
[46] P. Collin, N. Matsumura, A. Lädermann, P.J. Denard, G. Walch, Relationship between massive chronic rotator cuff tear pattern and loss of active shoulder range of motion, J. Shoulder Elb. Surg. 23 (2014) 1195–1202, http://dx.doi.org/10.1016/j.jse.2013.11.019.
[47] A. Reddy, L.V. Gulotta, X. Chen, A. Castagna, D.M. Dines, R.F. Warren, A. Kontaxis, Biomechanics of lower trapezius and latissimus dorsi transfers in rotator cuff-deficient shoulders, J. Shoulder Elb. Surg. 28 (2019) 1257–1264, http://dx.doi.org/10.1016/j.jse.2018.11.066.